ARTICLE   OPEN

Probing the interfacial coupling in ternary van der Waals heterostructures

Heng Wu [1,2], Miao-Ling Lin[1], Yu-Chen Leng[1], Xue Chen[1,2], Yan Zhou[1], Jun Zhang [1,2] and Ping-Heng Tan [1,2 ✉]

Good interfacial coupling between each constituent of van der Waals Heterostructures (vdWHs) is the prerequisite for the distinguished performance of related devices. Since vdWHs-based devices commonly consist of three or more constituents, an effective evaluation of interfacial coupling quality in multiple heterointerfaces is critical during the device fabrication process. Here, in ternary vdWHs composed of hBN, graphene (Gr) and transition metal dichalcogenide (TMD) flakes, which are essential building blocks for low-dimensional vdWHs-based electronic and optoelectronic devices, we realized probe and quantification of the interfacial coupling by low-frequency Raman spectroscopy under resonant excitation through the C exciton energy in TMD constituents. Based on the frequencies of emerging interlayer vibration modes in hBN/TMD/Gr ternary vdWHs, the interfacial coupling force constants of hBN/TMD and TMD/Gr interfaces are estimated as parameters to quantitatively evaluate the interfacial coupling strength at the corresponding interfaces. Moreover, the interfacial coupling strength at Gr/hBN interface is also successfully revealed in Gr/hBN/MoTe$_2$ ternary vdWHs, which cannot be directly characterized from Gr/hBN binary vdWH due to its unobservable interlayer modes with weak electron-phonon coupling. This general strategy can be further extended to probe and quantify the interfacial coupling quality in polynary vdWHs and related devices.

INTRODUCTION

Van der Waals heterostructures (vdWHs) with atomically clean interfaces provide an ideal platform for fundamental studies and novel device demonstration[1–6]. With the development of integration techniques, the structure of vdWHs becomes complicated. Polynary vdWH composed of a semiconducting channel, metallic contacts or an insulating dielectric/encapsulation, has already become a basic paradigm in related electronic and optoelectronic device engineering[7]. Transition metal dichalcogenides (TMDs), graphene (Gr) and hexagonal boron nitride (hBN), which usually correspond to the three roles, in turn, have naturally become essential building blocks in vdWHs-based devices. These constituents in vdWHs are coupled together by van der Waals interaction, which induces the interfacial coupling for emerging superior properties. For instance, metal-insulator transition was realized in hBN-encapsulated MoS$_2$/Gr vdWHs-based field-effect transistors owing to the barrier-free contact between the graphene electrode and MoS$_2$[8]. Tunnel diodes consisting of a graphene electrode, hBN tunnel barrier layer, and an electrostatically gated monolayer WS$_2$ layer exhibit efficient carrier-to-exciton conversion and planar electroluminescence[6]. Furthermore, issues in interfacial coupling induced by stacking sequence[9], constituent thickness[10,11], and twist angle between the two adjacent constituents[1,2,12,13] also significantly influence the physical properties of vdWHs and further affect the related device performance. Therefore, the understanding of the interfacial coupling between constituents in vdWHs is critical to achieve demanded performance of novel vdWHs-based devices.

A variety of optical and electrical techniques have been used to characterize the interlayer coupling in layered systems[10,13–15]. Among them, low-frequency (LF) Raman spectroscopy can directly detect the interlayer vibration modes, i.e., shear (S) modes and layer-breathing (LB) modes in layered materials[14,16]. Using the frequencies of the measured S or LB modes, the relevant force constants can be obtained based on the linear chain model (LCM), and then the interlayer coupling strength can be estimated quantitatively[14]. In binary vdWHs, additional interlayer vibration modes have been observed due to the interfacial coupling between the constituents[17–19]. The interfacial coupling in Gr/TMD and hBN/TMD binary vdWHs has been revealed by probing the corresponding interlayer vibration modes[18–20]. The understanding and manipulation of the interlayer phonon behavior in vdWHs also contribute to the optimization of electrical and thermal transport properties in the related devices[21]. Nowadays, ternary and even polynary vdWHs have become the mainstream structure of low-dimensional electronic and optoelectronic devices; however, the quantitative evaluation of the corresponding interfacial coupling quality is still a critical issue in device fabrication to ensure the stability of device performance.

Here we proposed a general approach to probe and quantify the interfacial coupling in ternary vdWHs composed of graphene, hBN and TMDs, by measuring the LF Raman spectroscopy under excitation in resonance with C exciton energy of the TMD constituents. The LB modes in ternary hBN/TMD/Gr vdWHs as compelling features of interfacial coupling can be clearly observed. The interfacial LB force constants of hBN/TMD and Gr/TMD interfaces were uniquely determined by the LCM. Good consistency of all reproduced results and the experimental frequencies of LB modes validates the applicability of the LCM in ternary vdWHs. Furthermore, as a typical structure with unobservable LB modes, Gr/hBN vdWHs were assembled with 2H-MoTe$_2$ flakes into Gr/hBN/MoTe$_2$ ternary vdWHs, where the LB modes can be observed owing to the strong coupling of LB modes to the excitons in MoTe$_2$ constituent. Based on the emerging LB

[1]State Key Laboratory of Superlattices and Microstructures, Institute of Semiconductors, Chinese Academy of Sciences, Beijing 100083, China. [2]Center of Materials Science and Optoelectronics Engineering & CAS Center of Excellence in Topological Quantum Computation, University of Chinese Academy of Sciences, Beijing 100049, China. ✉email: phtan@semi.ac.cn
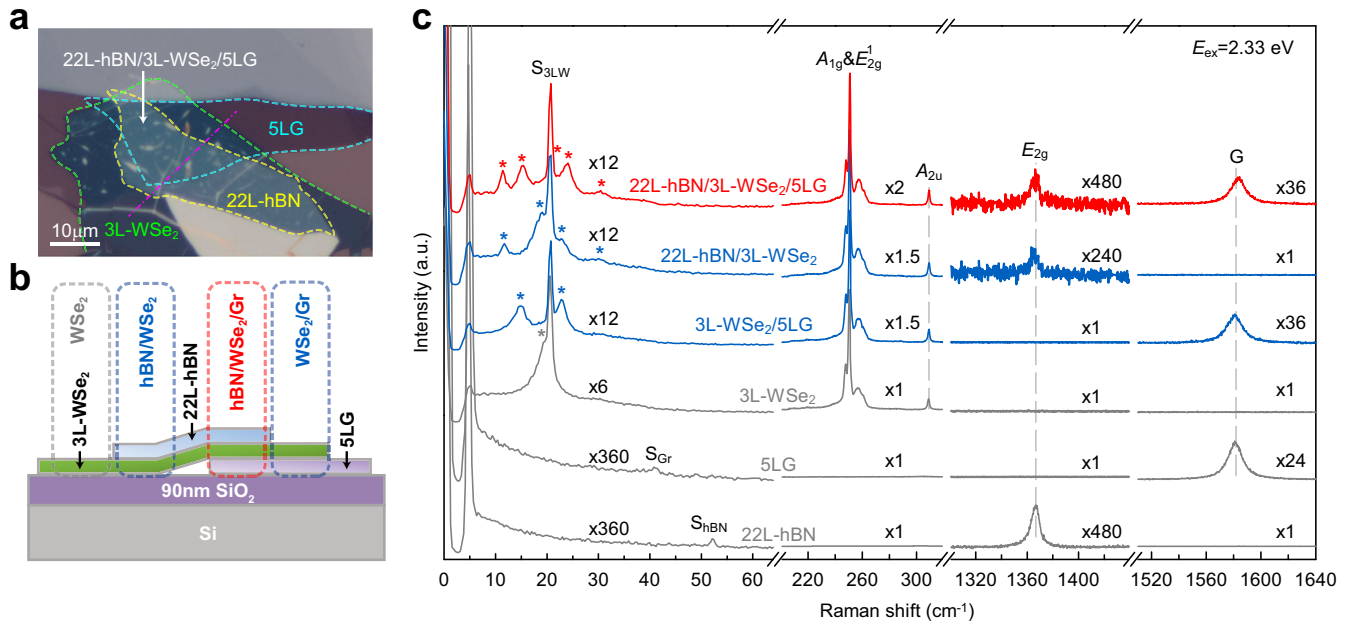
Fig. 1 Raman signatures of hBN/WSe₂/Gr vdWH and its constituents. a Optical image of the sample containing 22L-hBN/3L-WSe₂/5LG, 22L-hBN/3L-WSe₂, 3L-WSe₂/5LG, and 3L-WSe₂. **b** Schematic diagram of cross-section of the sample along the dash-dotted line in **a**. The regions of ternary vdWH, binary vdWHs, and pristine WSe₂ flakes are indicated. **c** Raman spectra of 22L-hBN, 5LG, 3L-WSe₂, 3L-WSe₂/5LG, 22L-hBN/3L-WSe₂, and 22L-hBN/3L-WSe₂/5LG. Stars indicate the LB modes. S_{3LW}, S_{Gr} and S_{hBN} denote the S modes of 3L-WSe₂, multilayer graphene and hBN flakes, respectively.

modes, the LB force constant at Gr/hBN interface was successfully obtained and the relative Raman intensity of the LB modes was well reproduced by the phonon wave function projection method.

RESULTS AND DISCUSSION

Interfacial coupling features in hBN/WSe₂/Gr ternary vdWHs

Novel electronic and optoelectronic devices based on vdWHs usually contain multiple constituents, in which TMD, hBN and graphene flakes are three common building blocks[5–8]. As a prototype of related devices, hBN/WSe₂/Gr ternary vdWHs were constructed via the dry transfer method using exfoliated hBN, graphene and WSe₂ flakes. The bottom k-layer graphene flake (kLG) was first transferred onto a 90 nm Si/SiO₂ substrate, followed by the n-layer WSe₂ flake (nL-WSe₂). The top m-layer hBN flake (mL-hBN) was then stacked above the WSe₂ flake so that a sample containing the mL-hBN/nL-WSe₂/kLG ternary vdWH can be fabricated (See Methods). In addition to the hBN/WSe₂/Gr ternary vdWH, hBN/WSe₂, WSe₂/Gr binary vdWHs along with individual hBN, WSe₂, and graphene flakes can generally be found at the side of the ternary vdWH. The rigid S and LB modes are the characteristic features of layered materials, whose peak positions vary with the number of layers[16]. Therefore, the number of layers of WSe₂ constituent in hBN/WSe₂/Gr ternary vdWHs can be directly confirmed by the peak positions of S and LB modes (Pos(S)&Pos(LB)) before transfer[22,23]. For hBN and graphene flakes, the number of layers can be obtained by atomic force microscope (AFM) or Raman intensity from substrate[24].

The sample containing 22L-hBN/3L-WSe₂/5LG ternary vdWH, 22L-hBN/3L-WSe₂, 3L-WSe₂/5LG, and 3L-WSe₂ was firstly investigated, whose optical microscope image is shown in Fig. 1a. Figure 1b illustrates the side view of the sample and marks out the regions of ternary, binary vdWHs and individual WSe₂. Figure 1c compares the Raman spectra of 22L-hBN, 5LG, 3L-WSe₂, 3L-WSe₂/5LG, 22L-hBN/3L-WSe₂, and 22L-hBN/3L-WSe₂/5LG under an excitation energy (E_{ex}) of 2.33 eV. Intralayer vibration modes in the high-frequency region (>100 cm⁻¹) are characteristic features

of each constituent, such as the A_{1g}, E_{2g}^1 and A_{2u} modes of 3L-WSe₂, the G mode of 5LG, and the E_{2g} mode of 22L-hBN[14,25,26]. Notably, here we denote the Raman modes according to the irreducible representations in the corresponding bulk counterparts for simplicity, although the lattice symmetries and notations should in principle vary with flake thickness and stacking sequence of vdWHs. In this region, the spectra of binary and ternary vdWHs are almost the sum of those of the corresponding individual hBN, graphene, and WSe₂ flakes. Pos(A_{1g}), Pos(E_{2g}^1)and Pos(A_{2u}) of 3L-WSe₂, Pos(G) of 5LG, and Pos(E_{2g}) of 22L-hBN are almost unchanged, which suggests that the intralayer vibration modes are not suitable to be the indicators for the interfacial coupling of vdWHs. Indeed, the interfacial coupling is much weaker than the intralayer bonding, so the frequency of intralayer vibration modes in vdWHs is not sensitive to the interfacial coupling between two constituents[27]. Apart from the high-frequency modes, low-frequency S and LB modes also exist in vdWHs, which are directly related to the interfacial shear and breathing coupling, respectively[18,19]. In the low-frequency spectral range (<60 cm⁻¹), the S mode of 3L-WSe₂ is observed in 22L-hBN/3L-WSe₂, 3L-WSe₂/5LG, and 22L-hBN/3L-WSe₂/5LG with almost the same peak position, which suggests that the S modes of vdWHs are localized within their constituents, similar to the previous results[18,19]. Only one LB mode can be observed in 3L-WSe₂, while more LB modes emerge in corresponding binary and ternary vdWHs, as marked by stars in Fig. 1c. Moreover, Pos(LB) in ternary vdWH is quite different from that in binary ones. These LB modes can be distinguished by polarized Raman spectroscopy, as shown in Supplementary Fig. 1. Since the LB modes originate from the interaction between rigid layers, this significant difference indicates the existence of the interfacial coupling between all adjacent constituents. To ensure the reliability of the results, Raman measurements were performed on multiple points within the homogeneous region (with no visible wrinkles or bubbles) of the sample, as shown in Supplementary Fig. 2. The different behaviors between S and LB modes result from their different interfacial coupling at the heterointerface, which had been clearly addressed in the case of twisted multilayer graphene beyond the
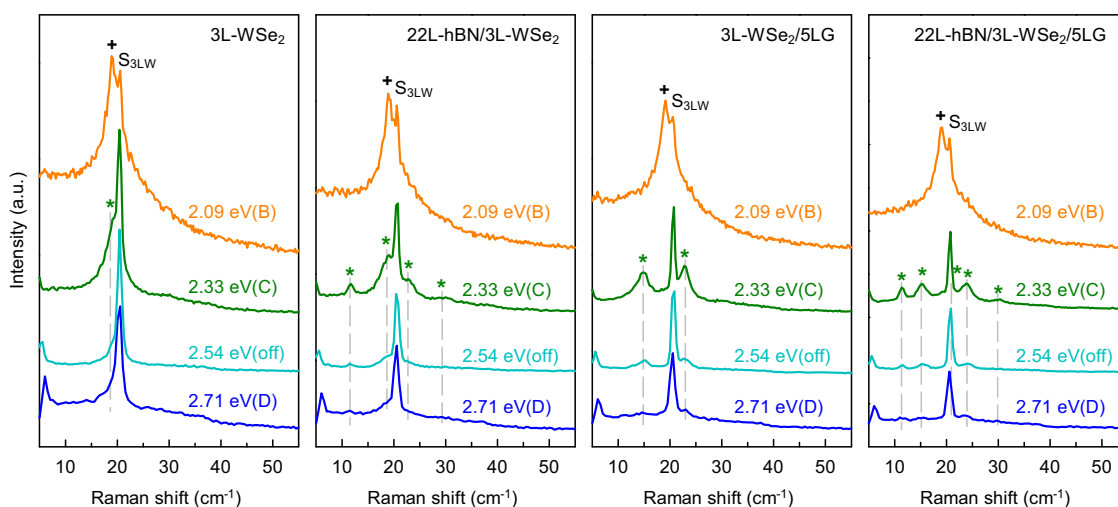
Fig. 2 Intensity resonances of LB modes in hBN/WSe₂/Gr vdWH and its constituents. LF Raman spectra of 3L-WSe₂, 22L-hBN/3L-WSe₂, 3L-WSe₂/5LG, and 22L-hBN/3L-WSe₂/5LG excited by four E_{ex}. The E_{ex} corresponding to B, C, and D exciton energies of 3L-WSe₂ are labeled in brackets. The stars indicate the LB modes and the crosses show TA phonon in WSe₂[30].

magic angle[12]: twisting forms periodic charge density and declines the interlayer shear coupling for a small displacement, while the mean charge densities are almost unchanged and keeps the interlayer breathing coupling comparable to that at Bernal-stacked interface. The charge density at the heterointerfaces of binary and ternary vdWHs exhibits similar behavior to that in twisted multilayer graphene, leading to the localized S modes and extended LB modes. Therefore, the emergence of additional LB modes is considered to be a direct fingerprint for the interfacial coupling in ternary vdWHs.

Probing the LB modes in TMD-based vdWHs under resonant excitation

As a feature of interfacial coupling in vdWHs, the existence of additional LB modes is critical for their quality analysis. The formation of vdWHs breaks the original symmetry of each constituent, leading to all the LB modes in vdWHs being Raman active. In the binary vdWHs such as hBN/TMD, whether these LB modes can be clearly observed in the Raman spectra of vdWHs or not depends on the strength of their coupling to the excitons of TMD constituent[19]. The LB modes in hBN/TMD binary vdWHs exhibit significant resonant behaviors similar to that in TMD constituent, which is mainly related to the electronic band structure[19]. In the following, we will discuss the case of hBN/TMD/Gr ternary vdWHs.

Figure 2 depicts the LF Raman spectra of 3L-WSe₂, 22L-hBN/3L-WSe₂, 3L-WSe₂/5LG, and 22L-hBN/3L-WSe₂/5LG excited by three specific E_{ex}, which correspond to the B (2.09 eV), C (2.33 eV), and D (2.71 eV) exciton energies of 3L-WSe₂, respectively[28,29]. An off-resonance case excited by 2.54 eV is also included for reference. The Raman intensity is normalized by the E_1 mode intensity of quartz at 127.0 cm⁻¹ at the corresponding E_{ex}. Among the four E_{ex}, the LB mode of 3L-WSe₂ is significantly enhanced at $E_{ex} = 2.33$ eV, i.e., the C exciton energy. Similar resonance effect of the LB modes in 22L-hBN/3L-WSe₂, 3L-WSe₂/5LG, and 22L-hBN/3L-WSe₂/5LG also emerges at $E_{ex} = 2.33$ eV. However, the LB modes of 3L-WSe₂ and the corresponding binary and ternary vdWHs can not be clearly distinguished from the background spectra at E_{ex} of 1.96 eV (B exciton energy) and 2.71 eV (D exciton energy). These LB modes are also very weak under off-resonant excitation conditions at $E_{ex} = 2.54$ eV. Therefore, in order to enable the clear observation of the LB modes in TMD-based vdWHs, the E_{ex} is necessary to match the C exciton energy of the TMD constituent. This is in agreement with the previous result on WS₂-based vdWHs[19].

Consequently, in the following experiments on WSe₂-, WS₂-, MoSe₂-, MoS₂-, and MoTe₂-based vdWHs, we also chose the E_{ex} corresponding to C exciton energies of these five TMD constituents, i.e., 2.33 eV for WSe₂[28], 2.71 eV for WS₂[28,30], MoSe₂[31,32], and MoS₂[33], and 2.54 eV for MoTe₂[34].

### Evaluation of interfacial coupling quality in hBN/TMD/Gr ternary vdWHs

The clear observation of additional LB modes in binary vdWH guarantees its good interfacial coupling. For a ternary vdWH, there exist two heterointerfaces corresponding to the two sets of adjacent constituents. The distinguished performance of the corresponding devices depends on the good interfacial coupling of the two heterointerfaces. In principle, with regard to any one binary vdWH corresponding to adjacent constituents, once additional LB modes are observed in the ternary vdWH, its good interfacial coupling can be confirmed. The LCM has been proved to directly link Pos(LB) with interlayer (or interfacial) coupling strength of pristine layered materials and binary vdWHs[14,18,19]. To quantitatively analyze the interfacial coupling strength in the ternary vdWH, it is necessary to extend it to ternary vdWHs beyond binary ones.

In the LCM, each rigid layer is treated as a ball with corresponding mass per unit area and the interaction between two layers is described by an effective force constant. Based on the LCM, for a vdWH with a certain number of layers of constituents, its Pos(LB) can be determined by a series of LB force constants within the vdWH, and vice versa. Thus, the interlayer (interfacial) LB force constants in vdWHs can be estimated according to the experimental Pos(LB).

We consider an A/B binary vdWH composed of mL-A and nL-B, assuming that the nearest-neighbor (m, $n > 1$) and second nearest-neighbor (m, $n > 2$) LB force constants involved in mL-A (nL-B) are $\alpha^{\perp}$(A) ($\alpha^{\perp}$(B)) and $\beta^{\perp}$(A) ($\beta^{\perp}$(B)), respectively. For simplicity, only the nearest-neighbor LB force constant is considered at the A/B interface, i.e., $\alpha^{\perp}$(A/B). Pos(LB) (in cm⁻¹) in mL-A/nL-B can be calculated by solving a $N \times N$ ($N = m + n$) tridiagonal linear homogeneous equation:

$$\omega_i^2 \mathbf{M} \mathbf{u_i} = \frac{1}{4\pi^2 c^2} \mathbf{D} \mathbf{u_i}, \tag{1}$$

where $\mathbf{u_i}$ is the phonon eigenvector of the ith mode with frequency ω_i. $\mathbf{M}$ is the diagonal mass matrix of the vdWH, in which element M_{ii} is the mass per unit area of ith layer and $M_{ij} = 0$ ($i \neq j$).
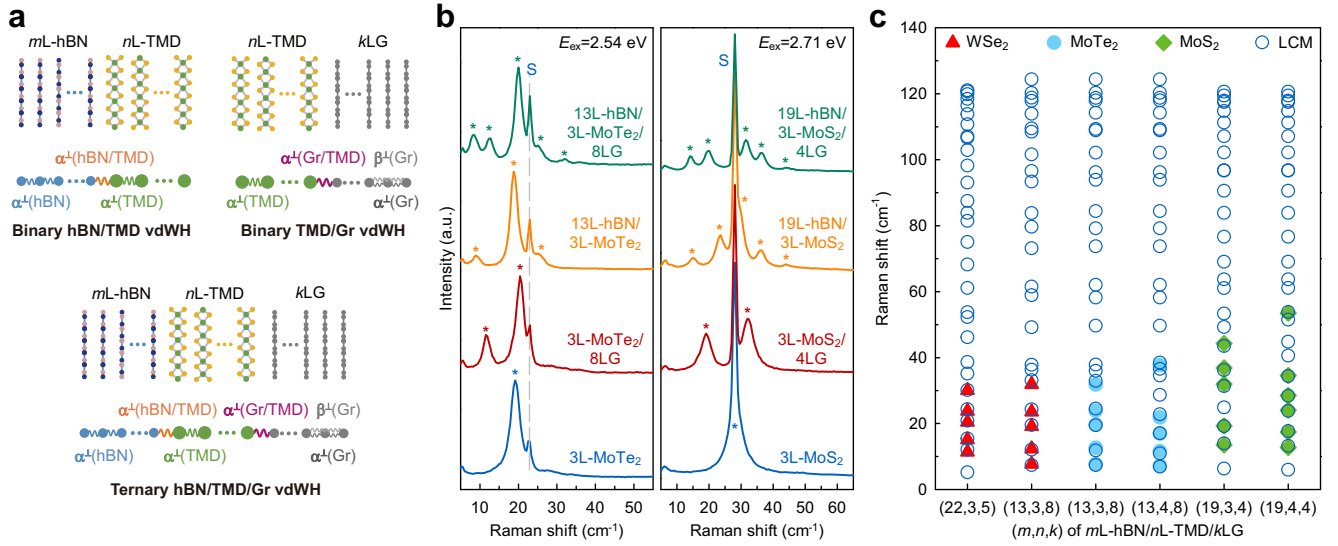
Fig. 3 LB modes in binary and ternary TMD-based vdWHs. a Schematic diagram of LCM for hBN/TMD, TMD/Gr, and hBN/TMD/Gr vdWHs. **b** LF Raman spectra of 13L-hBN/3L-MoTe$_2$/8LG, 19L-hBN/3L-MoS$_2$/4LG, and their corresponding binary hBN/TMD, TMD/Gr vdWHs and individual TMD flakes. **c** Calculated (hollow circles) and experimental (filled symbols) Pos(LB) in mL-hBN/nL-TMD/kLG vdWHs (TMD = WSe$_2$, MoTe$_2$, and MoSe$_2$). Indexes (m, n, k) represent the number of layers of the constituents in each vdWH.

$c = 3.0 \times 10^8$ m · s^{-1} is the speed of light. **D** is the LB force constant matrix, in which element D_{ij} ($i \neq j$) is the negative value of the LB force constant between ith and jth layers and $D_{ii} = -\sum_j D_{ij}$. Take 3L-A/3L-B as an example, **M** can be written as

$$\mathbf{M} = \begin{pmatrix} m(\mathrm{A}) & 0 & 0 & 0 & 0 & 0 \\ 0 & m(\mathrm{A}) & 0 & 0 & 0 & 0 \\ 0 & 0 & m(\mathrm{A}) & 0 & 0 & 0 \\ 0 & 0 & 0 & m(\mathrm{B}) & 0 & 0 \\ 0 & 0 & 0 & 0 & m(\mathrm{B}) & 0 \\ 0 & 0 & 0 & 0 & 0 & m(\mathrm{B}) \end{pmatrix}, \quad (2)$$

and **D** can be written as

$$\mathbf{D} = \begin{pmatrix} \alpha^{\perp}(\mathrm{A}) + \beta^{\perp}(\mathrm{A}) & -\alpha^{\perp}(\mathrm{A}) & -\beta^{\perp}(\mathrm{A}) & 0 & 0 & 0 \\ -\alpha^{\perp}(\mathrm{A}) & 2\alpha^{\perp}(\mathrm{A}) & -\alpha^{\perp}(\mathrm{A}) & 0 & 0 & 0 \\ -\beta^{\perp}(\mathrm{A}) & -\alpha^{\perp}(\mathrm{A}) & \alpha^{\perp}(\mathrm{A/B}) + \alpha^{\perp}(\mathrm{A}) + \beta^{\perp}(\mathrm{A}) & -\alpha^{\perp}(\mathrm{A/B}) & 0 & 0 \\ 0 & 0 & -\alpha^{\perp}(\mathrm{A/B}) & \alpha^{\perp}(\mathrm{A/B}) + \alpha^{\perp}(\mathrm{B}) + \beta^{\perp}(\mathrm{B}) & -\alpha^{\perp}(\mathrm{B}) & -\beta^{\perp}(\mathrm{B}) \\ 0 & 0 & 0 & -\alpha^{\perp}(\mathrm{B}) & 2\alpha^{\perp}(\mathrm{B}) & -\alpha^{\perp}(\mathrm{B}) \\ 0 & 0 & 0 & -\beta^{\perp}(\mathrm{B}) & -\alpha^{\perp}(\mathrm{B}) & \beta^{\perp}(\mathrm{B}) + \alpha^{\perp}(\mathrm{B}) \end{pmatrix}. \quad (3)$$

When the LCM is extended to 2L-A/2L-B/3L-C ternary vdWH, the corresponding **D** can be written as

$$\mathbf{D} = \begin{pmatrix} \alpha^{\perp}(\mathrm{A}) & -\alpha^{\perp}(\mathrm{A}) & 0 & 0 & 0 & 0 & 0 \\ -\alpha^{\perp}(\mathrm{A}) & \alpha^{\perp}(\mathrm{A}) + \alpha^{\perp}(\mathrm{A/B}) & -\alpha^{\perp}(\mathrm{A/B}) & 0 & 0 & 0 & 0 \\ 0 & -\alpha^{\perp}(\mathrm{A/B}) & \alpha^{\perp}(\mathrm{A/B}) + \alpha^{\perp}(\mathrm{B}) & -\alpha^{\perp}(\mathrm{B}) & 0 & 0 & 0 \\ 0 & 0 & -\alpha^{\perp}(\mathrm{B}) & \alpha^{\perp}(\mathrm{B}) + \alpha^{\perp}(\mathrm{B/C}) & -\alpha^{\perp}(\mathrm{B/C}) & 0 & 0 \\ 0 & 0 & 0 & -\alpha^{\perp}(\mathrm{B/C}) & \alpha^{\perp}(\mathrm{B/C}) + \alpha^{\perp}(\mathrm{C}) + \beta^{\perp}(\mathrm{C}) & -\alpha^{\perp}(\mathrm{C}) & -\beta^{\perp}(\mathrm{C}) \\ 0 & 0 & 0 & 0 & -\alpha^{\perp}(\mathrm{C}) & 2\alpha^{\perp}(\mathrm{C}) & -\alpha^{\perp}(\mathrm{C}) \\ 0 & 0 & 0 & 0 & -\beta^{\perp}(\mathrm{C}) & -\alpha^{\perp}(\mathrm{C}) & \beta^{\perp}(\mathrm{C}) + \alpha^{\perp}(\mathrm{C}) \end{pmatrix}. \quad (4)$$

Note that the second nearest-neighbor LB force constants are not applicable for 2L-A and 2L-B.

Usually, based on the previous reports, the nearest-neighbor LB coupling is enough to reproduce Pos(LB) in TMD, hBN and the related vdWHs[19,35,36]. However, the second nearest-neighbor LB force constant should be taken into account for multilayer graphene flakes[12,18]. Figure 3a depicts the schematic diagrams of LCM for hBN/TMD, TMD/Gr binary vdWHs, and hBN/TMD/Gr ternary vdWHs along with their corresponding LB force constants, i.e., $\alpha^{\perp}$(TMD), $\alpha^{\perp}$(hBN), $\alpha^{\perp}$(Gr), $\beta^{\perp}$(Gr), $\alpha^{\perp}$(hBN/TMD), and $\alpha^{\perp}$(Gr/TMD). Generally, $\alpha^{\perp}$(TMD) can be directly obtained from Pos(LB) in TMD flakes, whose LB modes are easily observed at E_{ex} matching to the C exciton energy. In contrast, the LB modes are unobservable in graphene and hBN flakes due to weak electron-phonon coupling, so that $\alpha^{\perp}$(hBN), $\alpha^{\perp}$(Gr), and $\beta^{\perp}$(Gr) can not be obtained directly from Raman spectra of pristine hBN and

Table 1. LB force constants of layered materials and heterointerfaces.

Layered Materials (X)	m(X) $(10^{-7}$ kg $\cdot$ m$^{-2})$	$\alpha^{\perp}$(X) $(10^{19}$ N $\cdot$ m$^{-3})$	$\beta^{\perp}$(X) $(10^{19}$ N $\cdot$ m$^{-3})$	$\alpha^{\perp}$(hBN/X) $(10^{19}$ N $\cdot$ m$^{-3})$	$\alpha^{\perp}$(Gr/X) $(10^{19}$ N $\cdot$ m$^{-3})$
graphene	7.56	10.7	0.95	7.83	/
hBN	7.54	9.88	/	/	7.83
MoS$_2$	30.2	8.65	/	8.63	5.68
MoSe$_2$	44.7	8.32	/	11.6	6.67
MoTe$_2$	53.2	7.75	/	12.8	4.24
WS$_2$	46.7	8.82	/	8.85	6.47
WSe$_2$	59.2	8.57	/	11.2	5.13

The nearest-neighbor ($\alpha^{\perp}$) and second nearest-neighbor ($\beta^{\perp}$) LB force constants of layered materials and the related vdWHs obtained from experimental Pos(LB) by the LCM. Mass per unit area of each layer of layered materials is given.
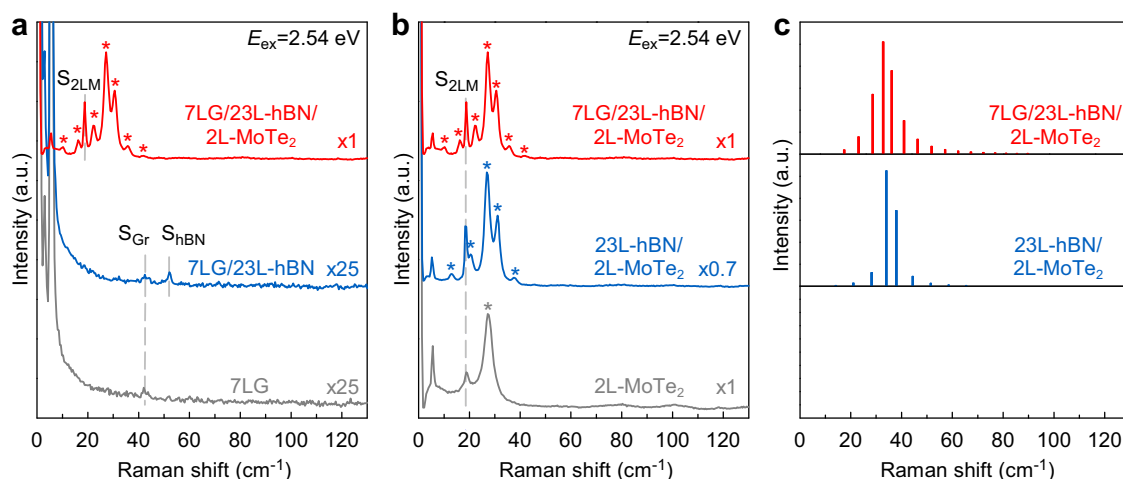
Fig. 4 Evolution of interlayer modes from individual constituents to Gr/hBN/MoTe$_2$ vdWH. a LF Raman spectra of 7LG, 7LG/23L-hBN, and 7LG/23L-hBN/2L-MoTe$_2$. **b** Raman spectra of 2L-MoTe$_2$, 23L-hBN/2L-MoTe$_2$, and 7LG/23L-hBN/2L-MoTe$_2$. **c** The calculated intensities of the LB modes in 23L-hBN/2L-MoTe$_2$ and 7LG/23L-hBN/2L-MoTe$_2$ based on the phonon wave function projection method[19]. The dashed lines and stars indicate Pos(S) and Pos(LB), respectively.

graphene flakes[14,26]. We used the following input parameters for LCM: $\alpha^{\perp}$(Gr) of 10.7×10^{19} N $\cdot$ m^{-3}, $\beta^{\perp}$(Gr) of 0.95×10^{19} N $\cdot$ m^{-3}, and $\alpha^{\perp}$(hBN) of 9.88×10^{19} N $\cdot$ m^{-3}, which are determined from twisted multilayer graphene and hBN/WS$_2$ vdWHs[12,19]. Therefore, only $\alpha^{\perp}$(hBN/TMD) and $\alpha^{\perp}$(TMD/Gr) are treated as fitting parameters in this work.

To confirm the applicability of LCM in ternary vdWHs, we fabricated several samples containing hBN/TMD/Gr, hBN/TMD, TMD/Gr vdWHs and individual TMD flakes, in which WSe$_2$, MoS$_2$ and MoTe$_2$ were used as TMD constituents (Supplementary Fig. 3). Six ternary vdWHs were obtained, including 22L-hBN/3L-WSe$_2$/5LG, 14L-hBN/3L-WSe$_2$/8LG, 14L-hBN/3L-MoTe$_2$/8LG, 14L-hBN/4L-MoTe$_2$/8LG, 19L-hBN/3L-MoS$_2$/8LG, and 19L-hBN/4L-MoS$_2$/8LG. The LF Raman spectra of hBN/TMD/Gr ternary vdWHs and the corresponding binary hBN/TMD, TMD/Gr vdWHs and individual TMD flakes are shown in Fig. 3b and Supplementary Fig. 4. Since there will be errors of ~0.5 nm (1–2 layers) for the thickness of hBN flakes measured by AFM, the number of layers of hBN flakes were finely tuned according to the residuals in the fitting process. We also fitted the interfacial LB force constants in binary vdWHs, which are found to be the same as that fitted in the corresponding ternary ones. In addition, other binary hBN/TMD, TMD/Gr vdWHs with different number of layers of constituents were prepared and their LF Raman spectra (Supplementary Fig. 5) were measured to reveal the corresponding LB force constants. All the fitted

interlayer/interfacial LB force constants are summarized in Table 1. The fitted values of $\alpha^{\perp}$(TMD) from pristine TMD flakes show good consistency with the previous reports[22,32,37–39]. Based on the fitted $\alpha^{\perp}$(hBN/TMD) and $\alpha^{\perp}$(Gr/TMD), all the LB modes in mL-hBN/nL-TMD/kLG can be calculated, as shown in Fig. 3c, well reproducing the experimental Pos(LB). In Fig. 3c, 14L-hBN/3L-MoTe$_2$/8LG and 14L-hBN/4L-MoTe$_2$/8LG exhibit distinct Pos(LB) from each other, although the change of its layer number of MoTe$_2$ constituent is only 1. Thus, the number of layers of TMD constituent in mL-hBN/nL-TMD/kLG can be reliably determined by LF Raman spectroscopy via measuring the LB modes of the corresponding vdWH.

It should be noted that the effect of the twist angle at the heterointerface on the interfacial LB coupling strength has not been considered. The lattice constants of hBN (0.251 nm) and graphene (0.247 nm) are similar, but they differ significantly from those of TMDs (>0.3 nm), so it is difficult to form moiré periodic structures at the heterointerfaces of TMD/hBN and TMD/Gr vdWHs which depend on twist angle. Therefore, the twist angle at the heterointerface does not remarkably modify the interfacial LB coupling strength and we cannot observe such difference through the frequencies of LB modes, which have been verified in MoS$_2$/Gr, WS$_2$/hBN, and MoTe$_2$/hBN vdWHs[18–20]. From the experimental perspective, our prepared samples have random interfacial twist angles for which we were able to obtain uniform interfacial

coupling strengths, so it indicates that the interfacial twist angle has less influence on the experiment results.

The above results confirm that the LCM can be extended to ternary vdWHs, and the unknown interfacial LB force constants at certain heterointerface within ternary vdWHs can be revealed by probing Pos(LB) in ternary vdWHs. Besides, interfacial LB force constants obtained from binary vdWHs can also be fully used to analyze experimental Pos(LB) in ternary ones. The above strategy could be extended for the evaluation of interfacial coupling quality in polynary vdWHs beyond ternary ones.

Interfacial coupling at Gr/hBN interface probed from Gr/hBN/MoTe$_2$ ternary vdWHs

For some binary vdWHs, the interlayer vibration modes are invisible in Raman spectra due to weak electron-phonon coupling, restricting the direct probe of their interfacial coupling. A typical example is the Gr/hBN vdWHs. The interfacial LB force constant at Gr/hBN interface, i.e., $\alpha^\perp$(Gr/hBN), has not been directly determined because the corresponding LB modes in Gr/hBN vdWHs have not been observed. However, when Gr/hBN binary vdWHs are assembled with TMD constituent to form Gr/hBN/TMD ternary vdWHs, the new LB modes may be observable due to the presence of cross-dimensional electron-phonon coupling[19] in Gr/hBN/TMD vdWHs, and $\alpha^\perp$(Gr/hBN) could be revealed from the experimental Pos(LB) based on the LCM for Gr/hBN/TMD vdWHs.

We fabricated several ternary Gr/hBN/MoTe$_2$ vdWHs by the same preparation method (Supplementary Fig. 6). The LF Raman spectra of 7LG, 7LG/23L-hBN, and 7LG/23L-hBN/2L-MoTe$_2$ are shown in Fig. 4a. The S mode of 7LG was observed in 7LG and 7LG/23L-hBN. Moreover, the S mode of 23L-hBN was also observed in 7LG/23L-hBN. LB modes of 7LG, 23L-hBN/7LG were not observed, since the frequencies of these modes calculated by the LCM should be less than 130 cm^{-1}. After assembling 7LG/23L-hBN with 2L-MoTe$_2$ to form 7LG/23L-hBN/2L-MoTe$_2$, a series of new LB modes was observed clearly in the ternary vdWH. This indicates the presence of interfacial coupling at the Gr/hBN interface, although the LB modes are absent in the 7LG flake and 7LG/23L-hBN vdWH. For comparison, the LB modes can be observed in 2L-MoTe$_2$, 23L-hBN/2L-MoTe$_2$, and 7LG/23L-hBN/2L-MoTe$_2$, as depicted in Fig. 4b. m and n were verified by the LCM based on the experimental Pos(LB) of mLG/kL-MoTe$_2$ and nL-hBN/kL-MoTe$_2$ binary vdWHs. LF Raman spectra of more samples were depicted in Supplementary Fig. 7. Taking $\alpha^\perp$(Gr/hBN) of 7.83×10^{19} N·m^{-3}, the calculated Pos(LB) for the six studied mLG/nL-hBN/kL-MoTe$_2$ vdWHs can reproduce the experimental Pos(LB) (Supplementary Fig. 8). This value is smaller than $\alpha^\perp$(hBN/MoTe$_2$) of 12.8×10^{19} N·m^{-3}, but larger than $\alpha^\perp$(Gr/MoTe$_2$) of 4.24×10^{19} N·m^{-3}. The determination of $\alpha^\perp$(Gr/hBN) from Gr/hBN/MoTe$_2$ ternary vdWHs indicates that the unknown interlayer LB force constant in a binary vdWH can be directly probed from the LB modes in the corresponding ternary vdWHs assembled from the binary vdWH and TMD flake as constituents.

In principle, mL-hBN/nL-TMD/kLG and mLG/nL-hBN/kL-MoTe$_2$ vdWHs show reduced symmetry than their individual constituents, and thus all the $(m + n + k - 1)$ LB modes of the ternary vdWHs become Raman active. However, only a few LB modes with frequencies close to that of LB modes in individual TMD constituents were observed, as depicted in Figs. 3b, 4b. In fact, the Raman intensity of the LB modes are related to their corresponding electron-phonon coupling strength. For example, the intensities of the LB modes in 23L-hBN/2L-MoTe$_2$ and 7LG/23L-hBN/2L-MoTe$_2$ can be calculated according to the phonon wave function projection method via cross-dimensional electron-phonon coupling[19], as the corresponding LB force constants are determined above. The calculated results are shown in Fig. 4c and in good agreement with the experimental data. Indeed, the calculation revealed that the LB modes with frequencies larger

than 60 cm^{-1} exhibit weak electron-phonon coupling strength, and thus cannot be observed in Raman spectra. This is the reason why Fig. 3c only shows the experimentally observed modes with frequencies below 60 cm^{-1} in different hBN/TMD/Gr ternary vdWHs. Therefore, the phonon wave function projection method via electron-phonon coupling proposed for binary vdWHs[19] can be extended to polynary ones to understand their Raman intensity of LB modes.

In summary, the interlayer Raman modes in hBN/TMD/Gr and Gr/hBN/TMD ternary vdWHs are investigated via Raman spectroscopy by selecting appropriate E_{ex} to resonate with C exciton in TMD constituents. The observed Pos(LB) in ternary vdWHs can be well understood by the LCM, which can serve as a critical indicator for interfacial coupling quality. The interfacial LB force constants at certain heterointerfaces in ternary vdWHs as parameters to evaluate the corresponding interfacial coupling strength were uniquely determined. The interfacial coupling at Gr/hBN interface was also revealed from Pos(LB) of Gr/hBN/MoTe$_2$ ternary vdWHs with different constituent layers, which is comparable with those at hBN/TMD and Gr/TMD interfaces. The relative Raman intensity of the LB modes in ternary vdWHs can be well reproduced by the phonon wave function projection method via electron-phonon coupling. This work provides a general approach to characterize the interfacial coupling strength in polynary vdWHs beyond binary ones.

METHODS

Sample preparation

Few-layer TMDs (WS$_2$, WSe$_2$, MoS$_2$, MoSe$_2$, and MoTe$_2$), hBN and graphene flakes were mechanically exfoliated from the corresponding bulk crystals (HQ graphene) onto polydimethylsiloxane (PDMS) sheets. The vdWHs was constructed layer by layer using the all-dry viscoelastic stamping method[40]. The flakes on PDMS were sequentially transferred onto 90 nm SiO$_2$/Si substrates in specific orders with the aid of an optical microscope and a nanomanipulator. The samples were annealed after the fabrication process under an ultrahigh vacuum (around 10^{-7} Pa) at 150 °C for 2 h to enhance the coupling between each constituent. The layer number of multilayer graphene flakes were determined by the intensity ratio between the Si peak from SiO$_2$/Si substrates underneath graphene flakes and that from bare SiO$_2$/Si substrates[24]. The layer number of TMD flakes were determined directly by the frequencies of their LB or S modes[16]. The thickness of hBN flakes was roughly measured using AFM, and then the precise layer number were deduced from the frequencies of LB modes in corresponding binary and ternary vdWHs based on the initial value obtained by AFM.

Raman measurements

Raman spectra were measured in a backscattering geometry at room temperature using a Jobin-Yvon HR800 micro-Raman system equipped with a liquid nitrogen-cooled charge-coupled detector (CCD) and a ×100 objective lens (numerical aperture = 0.9). The excitation energies are 2.09 eV from a He-Ne laser, 2.33 eV from a diode-pumped-solid-state laser, and 2.54 eV, 2.71 eV from an Ar$^+$ laser. The 2400 lines per mm grating was used in the Raman measurements, which enables each CCD pixel to cover 0.24 cm^{-1}, 0.33 cm^{-1}, 0.42 cm^{-1}, and 0.50 cm^{-1} at 2.09 eV, 2.33 eV, 2.54 eV, and 2.71 eV, respectively. Laser plasma lines were removed via BragGrate bandpass filters (OptiGrate Corp.). Measurements down to 5 cm^{-1} were achieved using three BragGrate notch filters (OptiGrate Corp.) with an optical density of 4 and with full width at half maximum of 5 ~10 cm^{-1} [14]. The laser power was kept below 0.2 mW to avoid sample heating.

DATA AVAILABILITY

CODE AVAILABILITY

REFERENCES

1. Tran, K. et al. Evidence for moiré excitons in van der Waals heterostructures. *Nature* **567**, 71–75 (2019).
2. Jin, C. et al. Observation of moiré excitons in WSe_2/WS_2 heterostructure superlattices. *Nature* **567**, 76–80 (2019).
3. Tang, Y. et al. Simulation of Hubbard model physics in WSe_2/WS_2 moiré superlattices. *Nature* **579**, 353–358 (2020).
4. Lee, G. H. et al. Flexible and transparent MoS_2 field-effect transistors on hexagonal boron nitride-graphene heterostructures. *ACS Nano* **7**, 7931–7936 (2013).
5. Cui, X. et al. Multi-terminal transport measurements of MoS_2 using a van der Waals heterostructure device platform. *Nat. Nanotechnol.* **10**, 534–540 (2015).
6. Wang, S. et al. Efficient carrier-to-exciton conversion in field emission tunnel diodes based on MIS-type van der Waals heterostack. *Nano Lett.* **17**, 5156–5162 (2017).
7. Liu, Y., Huang, Y. & Duan, X. Van der Waals integration before and beyond two-dimensional materials. *Nature* **567**, 323–333 (2019).
8. Liu, Y. et al. Toward barrier free contact to molybdenum disulfide using graphene electrodes. *Nano Lett.* **15**, 3030–3034 (2015).
9. Kim, K. et al. Band alignment in WSe_2 –graphene heterostructures. *ACS Nano* **9**, 4527–4532 (2015).
10. Fang, H. et al. Strong interlayer coupling in van der Waals heterostructures built from single-layer chalcogenides. *Proc. Natl. Acad. Sci. USA* **111**, 6198–6202 (2014).
11. Ubrig, N. et al. Design of van der Waals interfaces for broad-spectrum optoelectronics. *Nat. Mater.* **19**, 299–304 (2020).
12. Wu, J. B. et al. Interface coupling in twisted multilayer graphene by resonant Raman spectroscopy of layer breathing modes. *ACS Nano* **9**, 7440–7449 (2015).
13. Wang, K. et al. Interlayer coupling in twisted WSe_2/WS_2 bilayer heterostructures revealed by optical spectroscopy. *ACS Nano* **10**, 6612–6622 (2016).
14. Tan, P. H. et al. The shear mode of multilayer graphene. *Nat. Mater.* **11**, 294–300 (2012).
15. Zhao, Y. et al. Extraordinarily strong interlayer interaction in 2D layered PtS_2. *Adv. Mater.* **28**, 2399–2407 (2016).
16. Zhang, X. et al. Phonon and Raman scattering of two-dimensional transition metal dichalcogenides from monolayer, multilayer to bulk material. *Chem. Soc. Rev.* **44**, 2757–2785 (2015).
17. Lui, C. H. et al. Observation of interlayer phonon modes in van der Waals heterostructures. *Phys. Rev. B.* **91**, 165403 (2015).
18. Li, H. et al. Interfacial Interactions in van der Waals heterostructures of MoS_2 and graphene. *ACS Nano* **11**, 11714–11723 (2017).
19. Lin, M. L. et al. Cross-dimensional electron-phonon coupling in van der Waals heterostructures. *Nat. Commun.* **10**, 2419 (2019).
20. Nguyen, M. H., Lim, S. Y., Taniguchi, T., Wantanabe, K. & Cheong, H. Interlayer interaction in $2H$-$MoTe_2$/hBN heterostructures. *2D Mater.* **8**, 045004 (2021).
21. Kim, S. E. et al. Extremely anisotropic van der Waals thermal conductors. *Nature* **597**, 660–665 (2021).
22. Zhao, Y. et al. Interlayer breathing and shear modes in Few-Trilayer MoS_2 and WSe_2. *Nano Lett.* **13**, 1007–1015 (2013).
23. Li, X. L. et al. Determining layer number of two-dimensional flakes of transition-metal dichalcogenides by the Raman intensity from substrates. *Nanotechnology* **27**, 145704 (2016).
24. Li, X. L. et al. Layer number identification of intrinsic and defective multilayered graphenes up to 100 layers by the Raman mode intensity from substrates. *Nanoscale* **7**, 8135–8141 (2015).
25. Luo, X. et al. Effects of lower symmetry and dimensionality on Raman spectra in two-dimensional WSe_2. *Phys. Rev. B* **88**, 195313 (2013).
26. Stenger, I. et al. Low frequency Raman spectroscopy of few-atomic-layer thick hBN crystals. *2D Mater.* **4**, 031003 (2017).
27. Leng, Y. C. et al. Intrinsic effect of interfacial coupling on the high-frequency intralayer modes in twisted multilayer $MoTe_2$. *Nanoscale* **13**, 9732–9739 (2021).
28. Zhao, W. et al. Evolution of electronic structure in atomically thin sheets of WS_2 and WSe_2. *ACS Nano* **7**, 791–797 (2013).
29. Kim, S., Kim, K., Lee, J. U. & Cheong, H. Excitonic resonance effects and Davydov splitting in circularly polarized Raman spectra of few-layer WSe_2. *2D Mater* **4**, 045002 (2017).
30. Tan, Q. H. et al. Observation of forbidden phonons, Fano resonance and dark excitons by resonance Raman scattering in few-layer WS_2. *2D Mater.* **4**, 031007 (2017).
31. Arora, A., Nogajewski, K., Molas, M., Koperski, M. & Potemski, M. Exciton band structure in layered $MoSe_2$: from a monolayer to the bulk limit. *Nanoscale* **7**, 20769–20775 (2015).
32. Kim, K., Lee, J. U., Nam, D. & Cheong, H. Davydov splitting and excitonic resonance effects in Raman spectra of few-layer $MoSe_2$. *ACS Nano* **10**, 8113–8120 (2016).
33. Mak, K. F., Lee, C., Hone, J., Shan, J. & Heinz, T. F. Atomically thin MoS_2 : a new direct-gap semiconductor. *Phys. Rev. Lett.* **105**, 136805 (2010).
34. Ruppert, C., Aslan, O. B. & Heinz, T. F. Optical properties and band gap of single- and few-layer $MoTe_2$ crystals. *Nano Lett.* **14**, 6231–6236 (2014).
35. Zhang, X., Tan, Q. H., Wu, J. B., Shi, W. & Tan, P. H. Review on the Raman spectroscopy of different types of layered materials. *Nanoscale* **8**, 6435–6450 (2016).
36. Liang, L. et al. Low-frequency shear and layer-breathing modes in Raman scattering of two-dimensional materials. *ACS Nano* **11**, 11777–11802 (2017).
37. Zhang, X. et al. Raman spectroscopy of shear and layer breathing modes in multilayer MoS_2. *Phys. Rev. B* **87**, 115413 (2013).
38. Froehlicher, G. O. Unified description of the optical phonon modes in N -layer $MoTe_2$. *Nano Lett.* **15**, 6481–6489 (2015).
39. Yang, J., Lee, J. U. & Cheong, H. Excitation energy dependence of Raman spectra of few-layer WS_2. *FlatChem* **3**, 64–70 (2017).
40. Castellanos-Gomez, A. et al. Deterministic transfer of two-dimensional materials by all-dry viscoelastic stamping. *2D Mater.* **1**, 011002 (2014).

ACKNOWLEDGEMENTS

AUTHOR CONTRIBUTIONS

P.-H.T. conceived and supervised the project. H.W. prepared the samples and performed the experiments, assisted by Y.-C.L., X.C., Y.Z., and J.Z. H.W. and M.-L.L. analyzed the data. H.W. and P.-H.T. wrote the paper. All authors discussed the results.

COMPETING INTERESTS

The authors declare no competing interests.

ADDITIONAL INFORMATION